*Magn Reson Med*. Author manuscript; available in PMC 2021 October 01.

Published in final edited form as:

*Magn Reson Med*. 2020 October ; 84(4): 2161–2173. doi:10.1002/mrm.28242.

# Test-retest reliability and long-term stability of 3-tissue constrained spherical deconvolution methods for analyzing diffusion MRI data

**Benjamin T. Newman**[1,2,*], **Thijs Dhollander**[3], **Kristen A. Reynier**[4], **Matthew B. Panzer**[4], **T. Jason Druzgal**[1,2]

[1] Department of Radiology and Medical Imaging, School of Medicine, University of Virginia, Charlottesville, USA

[2] Brain Institute, University of Virginia, Charlottesville, USA

[3] Developmental Imaging, Murdoch Children's Research Institute, Melbourne, Australia

[4] Center for Applied Biomechanics, Department of Mechanical and Aerospace Engineering, University of Virginia, Charlottesville, USA

## Abstract

**Purpose:** Several recent studies have utilized a 3-tissue constrained spherical deconvolution pipeline to obtain quantitative metrics of brain tissue microstructure from diffusion-weighted MRI data. The three tissue compartments, comprising white matter-, grey matter-, and CSF-like (free water) signals, are potentially useful in the evaluation of brain microstructure in a range of pathologies. However, the reliability and long-term stability of these metrics has not yet been evaluated.

**Methods:** This study examined estimates of whole brain microstructure for the three tissue compartments, in three separate test-retest cohorts. Each cohort has different lengths of time between baseline and retest, ranging from within the same scanning session in the shortest interval to three months in the longest interval. Each cohort was also collected with different acquisition parameters.

**Results:** The CSF-like compartment displayed the greatest reliability across all cohorts, with intraclass correlation coefficient (ICC) values being above 0.95 in each cohort. White matter-like and grey matter-like compartments both demonstrated very high reliability in the immediate cohort (both ICC>0.90), however this declined in the 3-month interval cohort to both compartments having ICC>0.80. Regional CSF-like signal fraction was examined in bilateral hippocampus and had an ICC>0.80 in each cohort.

**Conclusion:** The 3-tissue CSD techniques provide reliable and stable estimates of tissue microstructure composition, up to 3 months longitudinally in a control population. This forms an important basis for further investigations utilizing 3-tissue CSD techniques to track changes in microstructure across a variety of brain pathologies.

---

[*] Correspondence to: Benjamin T. Newman, Department of Radiology and Medical Imaging, MR4, 409 Lane Rd, Charlottesville, VA 22903. bennewman3@gmail.com.

**Keywords**

microstructure; spherical deconvolution; diffusion; MRI; reliability

## Introduction

Diffusion-weighted Magnetic Resonance Imaging (dMRI) is a widely used, noninvasive, method for measuring the diffusion of water molecules in the brain. Within the microarchitectural environment of the brain, diffusion of water molecules is hindered by various cellular components, particularly the lipid bilayers that make up cell membranes. This principle has been applied to study white matter fiber bundles (“tracts”), as the myelin sheaths surrounding neuronal axons result in anisotropic diffusion(1,2,3). dMRI has seen widespread use in studies of brain connectivity as well as in clinical populations and neurosurgery(4,5,6,7).

Initially, anisotropic diffusion was typically modelled using a tensor, which sought to quantify both the average orientation, anisotropy, and magnitude of diffusion within each voxel of the brain; this approach is known as Diffusion Tensor Imaging (DTI)(1). More recently, the dMRI modelling domain has seen a proliferation in novel, more advanced, mathematical methods for analyzing the diffusion-weighted signal. These methods aim to overcome several shortcomings of applying the relatively simplistic DTI model to the complex diffusion-weighted signals observed in the brain. This complexity primarily arises from two physiological qualities of the brain itself: the first being crossing fibers, where white matter (WM) tracts occupying the same voxel are oriented differently in space(8,9); and the second being the presence of other fluids and tissues, including cerebrospinal fluid (CSF) and grey matter (GM) and other cell bodies which “contaminate” the directional signal(10,11,12,13,14). These are major issues as it has been estimated that up to 90% of WM tissue voxels contain more than one WM fiber tract orientation(15), and partial voluming effects alone ensure that a substantial number of voxels contain proportions of multiple tissue and/or fluid compartments(12,13,16).

To address these issues, and with the advent of high angular resolution diffusion imaging (HARDI) acquisition protocols, more advanced methods for describing the observed dMRI data have been proposed by a number of researchers(17,18,19). One such method, Constrained Spherical Deconvolution (CSD), allows for the presence of multiple fibers along different orientations(20). CSD resolves these orientations by deconvolving the signal profile corresponding to a prototypical single fiber-like voxel (termed a response function) from the observed signal in each and every other voxel, resulting in the orientation of fibers as a continuous angular function termed the Fiber Orientation Distribution (FOD). Quantitative information can also be obtained from the FOD, as a measure of “Apparent Fiber Density” (AFD) for each fiber population(21).

The original (“single-tissue”) CSD has been expanded into Multi-Shell Multi-Tissue CSD (MSMT-CSD) by performing a similar deconvolution with 3 separate WM, GM, and CSF-like tissue response functions. The approach was initially aimed at separating signal originating from GM and CSF-like tissue compartments, in order to improve the accuracy of the WM FOD itself, which otherwise appears very noisy (with many false positive “peaks” or lobes) when using single-tissue CSD in areas of partial voluming with other tissues and fluids(12,13,22). This subsequently benefits several other analysis and processing steps, such as streamline tractography, which heavily rely on a “clean” and accurate WM FOD. MSMT-CSD thus attempted to address the main shortcomings of the DTI model as well as additional remaining shortcomings of single-tissue CSD.

As its name hints at, MSMT-CSD requires a *multi-shell* diffusion acquisition scheme in order to successfully tease apart contributions from the 3 WM-, GM- and CSF-like compartments at once. However, to obtain the same benefits offered by MSMT-CSD, yet using only *single-shell* data, Dhollander & Connelly(23), have proposed a novel approach named Single-Shell 3-Tissue CSD (SS3T-CSD) that can resolve the WM-, GM- and CSF-like compartments as well. By relying only on *single-shell* data, it allows for shorter acquisition times and is compatible with a wider range of data, both historical as well as clinical.

Resolving these different compartments using either 3-tissue CSD method (i.e., MSMT-CSD or SS3T-CSD) holds value beyond improving WM tractography: it can also serve as a proxy for the evaluation of brain microstructure and tissue composition(24,25,26). By interrogating brain voxels for diffusion signal patterns that look ‘like’ compositions of the diffusion signals represented by the WM/GM/CSF response functions, it might be possible to gain quantifiable information about microstructure (Figure 1). Using these basic compartments as a diffusion signal model focuses more on coarse properties of brain tissue microstructure rather than separating similar cell types (e.g. different populations of glial cells), or separating different types of pathology (e.g. edema, CSF-infiltration in neurodegeneration, and damage from ischemic stroke). Although, provided with a known context, reasonable inferences of such pathology might be possible to make nonetheless. Even for WM tractography in cases of infiltration by pathological tissues, the 3-tissue CSD approach can provide direct benefits in terms of recovering healthy WM structures, e.g. in infiltrating tumors(27).

3-tissue CSD derived compartments are a promising, non-invasive method for exploring tissue composition in the brain. The utilization of this approach toward analyzing tissue composition might hold advantages over tensor-based models such as Free Water Elimination (FWE)(28). The free water estimate from the FWE technique was shown to have limited reproducibility: errors ranged from 5.2–18.2% across ROIs in a test-retest cohort(29). The CSF-like compartment from 3-tissue CSD techniques might provide an alternative way to recover free water contribution to the signal, using a WM model that does take into account crossing fibres (as opposed to a tensor method). With the advances provided in SS3T-CSD, it is also able to provide signal contribution from the full 3 tissue compartments using *single-shell* data (i.e. equivalent to acquisition requirements for the FWE technique), allowing for a broader range of input data compared to other 3-tissue compartment models such as NODDI (30). In a recent review of microstructural diffusion imaging applied to psychiatric disorders, Pasternak et al.(31), illustrated the acquisition sequence complexity compared to the number of microstructure compartments evaluated for several common dMRI analysis techniques. Addition of MSMT-CSD and SS3T-CSD illustrate the range of data required for input to a range of models and the capabilities of resolving compartments compared to other techniques (Figure 2).

To date, there has not been a quantitative test-retest study examining the reliability and long-term stability of 3-tissue CSD techniques. The purpose of this study is to provide evidence that 3-tissue CSD techniques are a reliable and stable approach for assessing brain microarchitecture, via analysis of the 3 resulting tissue signal fractions.

## Methods

### Cohorts:

Three test-retest cohorts were retrospectively evaluated in this study: two local datasets collected at the University of Virginia from ongoing research projects, and one publicly available dataset obtained from the Nathanial Kline Institute for Psychiatric Research: enhanced test-retest (eNKI-TRT) as part of the 1000 Functional Connectomes Project(32,33,34). Both studies collected at the University of Virginia received ethical approval from the University of Virginia Institutional Review Board for Health Sciences Research. Each cohort has different time intervals between baseline and retest scans, and was collected with different acquisition parameters. This approach allows reliability to be measured under conditions that represent a variety of different diffusion imaging parameters. Examining stability across different time periods allows for insight into the potential for longitudinal studies tracking changes in 3-tissue signal fractions in individuals or between groups over time.

The first cohort ("*immediate rescan*" cohort) examined immediate test-retest reliability by performing identical dMRI acquisitions sequentially without table repositioning. This cohort consisted of individuals participating in a separate study at the University of Virginia that included multiple scanning sessions. The cohort consisted of 20 healthy control participants (all male, age at baseline 22.8±3.0 SD). Each participant was scanned twice at each of 3 visits (with the exception of one participant who only attended 2 scans) for a total of 59 baseline-rescan pairs collected for analysis.

The second cohort ("*short timescale*" cohort) is representative of the quality of diffusion imaging found in large-scale, open science cohorts. Subjects were selected from the original NKI Rockland community study, a group intentionally recruited for similarity to the demographics of the broader United States as a whole(34). 20 subjects (5 female, age at baseline: 34.4±12.9 SD) had diffusion MRI data available at both baseline and rescan. All participants were rescanned within a range of 7–60 days after baseline. Subjects were *not* excluded for any history of illness, and 2 participants had a diagnosed history of prior alcohol abuse while 2 other participants had a diagnosed history of a major depressive disorder. Both of these diagnoses are known to affect brain function and structure(35,36); but the nature of the within-subjects design did not necessitate removing any individuals from the study.

The third cohort ("*long timescale*" cohort) was collected as a healthy control group for a previously published study conducted at the University of Virginia examining college athletes(37). 52 participants (all male, age at baseline: 21.9±3.3 SD) were re-scanned 3–4 months after baseline (mean days between scans: 107.9±7.1 SD) and were screened for a history of neurologic disease or concussion.

## Image Acquisition:

As discussed previously, data from the three cohorts were acquired using different protocols.

The *immediate rescan* cohort was scanned using a Siemens Prisma 3T scanner with an isotropic voxel size of 1.7×1.7×1.7mm$^3$, TE=70ms and TR=2900ms; using a multi-shell protocol, 10 b=0 images and 64 gradient directions at both b=1500s/mm$^2$ and b=3000s/mm$^2$ were acquired. This protocol was applied twice with one immediately following the other without actively repositioning the participant in the scanner.

The *short timescale* cohort was acquired externally and obtained through the Neuroimaging Tools and Resources Collaboratory at www.nitrc.org. Imaging data was collected using a Siemens Trio Tim with an isotropic voxel size of 2×2×2mm$^3$, TE=85ms and TR=2400ms. Using a single-shell protocol, 9 b=0 images and 127 gradient directions at b=1500s/mm$^2$ were acquired.

The *long timescale* cohort was scanned using the same Siemens Prisma 3T scanner as the first (immediate rescan) cohort using a different protocol with an isotropic voxel size of 2.7×2.7×2.7mm$^3$, TE=100ms. Using a multi-shell protocol, 1 b=0 image and 30 gradient directions at both b=1000s/mm$^2$ and b=2000s/mm$^2$ were acquired.

## Analysis:

Data preprocessing was largely identical across all images in all cohorts in the study. Images were first denoised via use of the “dwidenoise” command in Mrtrix3(38). Gibbs ringing was then corrected, also using MRtrix3(39). This was followed by utilizing the FSL package (*“topup”* and *“eddy”*) to correct for susceptibility induced (EPI) distortions, eddy currents, and subject motion including the –repol flag to perform a Gaussian replacement of outliers (40,41,42,43). Finally, using MRtrix3 we upsampled the preprocessed data to 1.3×1.3×1.3mm$^3$ isotropic voxels(44,45,46). These preprocessing steps are largely similar to those used in other recently published works(46,47,26,27). A description of a basic single subject pipeline for performing SS3T-CSD, including these preprocessing steps, is available at https://3tissue.github.io/doc/single-subject.html. Brain masks were obtained for all subjects by performing a recursive application of the Brain Extraction Tool(48).

For 3-tissue CSD processing, the 3-tissue response functions were obtained from the data themselves using an unsupervised method(49), resulting in the single-fiber WM response function as well as isotropic GM and CSF response functions for each subject. For each tissue type (WM, GM, CSF), the response function was averaged across all individuals in each cohort to obtain a single unique set of 3-tissue response functions per cohort. For the *multi-shell* data in the immediate rescan and long timescale cohorts, MSMT-CSD was performed(22). For the *single-shell* data in the short timescale cohort, SS3T-CSD was performed(23). For all subjects in all cohorts, this resulted in their WM-like compartment (represented by a complete WM FOD) as well as GM-like and CSF-like compartments. The

CSF-like compartment can in this context also be interpreted as a free-water (FW) compartment(24). Finally, each subject's three tissue compartments were then normalised to sum to 1 on a voxel-wise basis, resulting in the final 3-tissue signal *fraction* maps(26); the metrics for which we performed the test-retest analyses in this work.

To measure the mean squared difference between baseline and rescan for each of the three tissue compartments, a cohort-specific template was first produced. This was achieved using an affine, followed by a non-linear registration guided by the WM FODs themselves in an unbiased manner (50). The warp that registered each subject's WM FODs to the template was then also applied to the WM-like, GM-like, and CSF-like maps, allowing all three tissue maps to be registered to the same template space and the mean squared difference between baseline and rescan to be calculated. CSF-like (free water) signal fraction in the hippocampus of each subject was measured in each subject relying on these same cohort-specific templates. A whole brain WM image from the LONI atlas(51) was registered along with each hippocampus map to the template using the ANTs image registration toolbox 'SyN' algorithm (52) and then subsequently warped to each individual scan using the reverse transform from template creation. In native space an average was computed of the CSF-like (free water) signal fractions in the ROI, using only voxels with a CSF-like signal fraction smaller than 0.5, to mimic free water analysis (i.e., to avoid accidentally including voxels outside of the brain parenchyma, which might be entirely CSF-filled spaces).

All processing was performed using a combination of different software packages: MRtrix3(53), MRtrix3Tissue (https://3Tissue.github.io, a fork of MRtrix3), FSL(54), ANTs(52).

## Results

The CSF-like (free water) tissue signal fraction map was restricted to voxels where the corresponding WM and GM signal maps summed to greater than 50%. This allowed for analysis of the CSF-like signal fraction in tissue without including the ventricles or subarachnoid space, the bulk size of which would otherwise bias a proper whole-brain free water measurement. Additionally, the CSF-like infiltration into brain tissue is a potentially more interesting measurement in the context of healthy functioning or pathology; and is indeed designed to be comparable to measurements of free water encountered in the literature(28). For all cohorts, results from the 3-tissue signal fractions were averaged across the brain parenchyma. Averages for baseline and retest values were compared by calculating the intraclass correlation coefficient (ICC) and Pearson's correlations. The results for both of these measures are summarized in Table 1.

Specific test-retest correlations for each of the three tissue types derived from the 3-tissue CSD techniques are presented in Figures 3–5. All correlations between baseline and retest were significant in all cohorts; the highest whole brain ICC values were obtained from the *immediate rescan* cohort (Figure 3). In the *short timescale* cohort, similar to the immediate rescan cohort, all compartments had an ICC value above 0.95 and Pearson's Rho above 0.90 (Figure 4). The *long timescale* cohort had slightly declined performance, yet with the ICC value for all compartments still being larger than 0.80 (Figure 5). To test the potential significance of this decline, bootstrapping of ICC values from each tissue type and cohort was performed to generate 95% confidence intervals after 100,000 bootstrap iterations. The 95% confidence interval generated from the long-timescale GM-like and WM-like signal fractions did not overlap with the confidence interval from both the immediate-rescan and short-timescale GM-like and WM-like signal fraction ICCs. The 95% confidence intervals from the CSF-like signal fraction ICCs from each cohort did overlap (Figure 6).

Additionally the mean squared difference was calculated for each tissue signal fraction map between each subject's baseline and rescan. This showed results largely consistent with overall whole brain averages of the signal fraction maps: each signal fraction map showed good reliability, with the CSF-like map having a mean squared difference less than 0.01 in each cohort, the GM-like map having a mean squared difference less than 0.025 in each cohort, and the WM-like map having a mean squared difference less than 0.035 in each cohort (Figure 7).

In each cohort, the hippocampi were also analyzed separately in order to demonstrate the utility of a 3-tissue CSD approach in a specific region of interest. Bilateral hippocampus was selected for this demonstration as a commonly studied brain ROI with representation from each of the three tissue compartments examined. Comparison of average CSF-like (free water) signal fraction in this ROI between baseline and retest resulted in an ICC value above 0.90 in both left and right hippocampus, as well as a significant Pearson's correlation (Figure 8A). In the *short timescale* cohort both left and right hippocampus similarly had an ICC value above 0.90 and a significant Pearson's correlation (Figure 8B). In the *long timescale* cohort both hippocampus had an ICC value above 0.80 and a significant Pearson's correlation (Figure 8C).

There was a consistent asymmetrical effect observed between the CSF-like signal fraction in right and left hippocampus across all cohorts. The CSF-like signal fraction in each subject's right and left hippocampus were averaged between baseline and rescan and a paired t-test performed for each cohort. This showed that there was a significantly greater CSF-like signal fraction in the right versus the left hippocampus ($T_{58} = -10.022$, $p<0.001$; $T_{19} = -6.002$, $p<0.001$; and $T_{51} = -23.486$, $p<0.001$; for the immediate rescan, short timescale, and long timescale cohorts, respectively).

## Discussion

Each of the 3-tissue signal fractions demonstrated good reliability across all of the measured timescales we assessed in this work. ICC values were above 0.95 for each of the tissue compartments included in the *immediate rescan* and *short timescale* cohorts. This occurred despite the *short timescale* cohort being *single-shell* data, a b-value of 1500, and a lower voxel size compared to the other two cohorts (both of which were *multi-shell* and had highest b-value of b=3000s/mm$^2$ and b=2000 s/mm$^2$ for the *immediate timescale* and *long timescale* cohorts, respectively). This result suggests that 3-tissue CSD techniques can reliably obtain quantitative measurements across a range of diffusion imaging protocols, including from openly available datasets. This performance, however, declined slightly in the *long timescale* cohort: the CSF-like (free water) signal fraction within tissue still had an

ICC value above 0.95 while the WM-like and GM-like signal fractions had a slightly lower ICC value, which bootstrapping indicated did not overlap with the 95% confidence intervals from the immediate or short-timescale cohorts. Regardless, all Pearson's correlations were highly significant, indicating that 3-tissue CSD techniques are still able to obtain reliable measurements of brain tissue microstructure, stable up to 3 months from baseline.

In our study it was observed that the reliability of the WM-like signal fraction maps declined in the long timescale cohort compared to the immediate and short-term rescan cohorts as measured by both bootstrapping of ICCs and by analysis of the mean squared difference. It is also possible that the lower number of gradient directions at each non-zero b-value in the long timescale cohort, compared to the other cohorts, caused the estimation of WM FODs to be more variable between rescans. Given the methodology employed for generating response functions and FODs, it would be expected that the ability to distinguish between WM and GM would be more dependent on angular resolution and contrast, while CSF would be more dependent on contrast between b-value shells. This may be supported by the observation that the CSF-like signal fraction map still had a high ICC which bootstrapping indicated was within the 95% confidence interval of both other cohorts. Given the nature of our datasets and the differences in site, acquisition, and subject cohorts, it is not possible to precisely disentangle each of these contributing factors.

The free water signal fraction additionally demonstrated good reliability in both hippocampi at each of the examined timescales. ICC values were above 0.80 and a significant effect of laterality was observed consistently across each cohort, with the right hippocampus having a significantly higher free water signal fraction than the left hippocampus. Though this study does not suggest any hypothesis for why this laterality was observed, it is consistent with volumetric MRI findings that demonstrate hippocampal asymmetry(55), as well as a recent study that reported asymmetry in hippocampal free water content(56). That study reported a 1% higher free water content in the right hippocampus compared to the left hippocampus of healthy controls, remarkably similar to the significantly different average observed in this study (0.9% in the *immediate timescale* cohort, 0.7% in the *short timescale* cohort, and 1.5% in the *long timescale* cohort, with higher free water signal fraction in the right hippocampus in each cohort). This suggests that free water signal fraction is both a reliable quantitative measurement for subcortical ROIs, and that it may be able to detect meaningful microstructural properties of such regions.

Given the nature of the datasets and cohorts used in our study, we did not address the topic of reproducibility of tissue signal fractions between different diffusion acquisition methods, subject cohorts, especially cohorts of different age ranges and demographic compositions, and analysis protocols. Three different acquisition protocols were used in this study, each with different angular resolutions, b-value shells, and sequences. Also, two different 3-tissue CSD analysis methods were employed. Given the nature of our datasets and the intrinsic differences in site, acquisition, timescale, and subject cohorts, it is not possible to precisely disentangle each of these contributing factors retrospectively using the data available for this study nor do we believe that attempting to do so would provide robust estimates of variation. Prospectively designing a study to control for these factors would allow for these dimensions to be properly disentangled and the contributions to data variability from each to be determined.

More traditional neuroimaging techniques do not provide quantifiable data on tissue microstructure, however this study has demonstrated a reproducible and reliable method for obtaining whole brain maps with quantifiable estimates of tissue microstructure. We observed these measures to be stable enough to be used in longitudinal studies lasting at least up to three months. They provide information on a voxel- or region-wise basis for analysis of subcortical structures, lesions, or developing brains(24,25,26,46). Related microstructural analysis of free water signal fractions has been performed in the context of Parkinson’s disease(57,58), Schizophrenia(59,60), and concussion(61). 3-tissue CSD techniques may thus have the potential to be applied to a variety of these and other neurological conditions.

3-tissue CSD derived tissue fractions provide a flexible framework for analyzing diffusion images in ways not addressed in this paper. While we examined the reliability of WM/GM/CSF-like tissue signal fractions here, other researchers have used response functions representing different tissue compartments when contextually appropriate. Pietsch et al.(47), applied two different WM response functions representing mature and immature WM in a developing adolescent cohort to observe WM maturation. Mito et al.(26), proposed to apply a statistical framework of compositional data analysis to analyze the full 3-tissue composition of WM-, GM- and CSF-like signal fractions directly to study microstructure in white matter lesions, following the initial suggestion of moving towards such WM/GM/CSF-like diffusion signal fraction interpretation by Dhollander et al.(24). In Aerts et al.(27), this idea was furthermore used for the purpose of disentangling WM FODs representing infiltrated WM tracts, in the presence of gliomas, so as to enable more reliable within-tumor tractography. Similar work has also recently been done by Chamberland et al.(62), who illustrated the use of 3-tissue signal fractions in the presence of cerebral metastases, both to assess their microstructure as well as to enable tractography through nearby edematous regions.

The relatively recent use of CSD to describe the diffusion signal(20) has led to some measure of controversy when compared to other established analysis techniques such as those based in multi-tensor models. One particular area of concern has been noted as the generation of ‘false-fibers’ on tracking algorithms due to spurious fODF peaks(63,64). Some studies using recent methodological improvements have suggested that the prevalence of false-fibers in CSD is oversold compared to other methods(65,66). In this study 3-tissue CSD demonstrated good reliability across all compartments. However as recent work has shown, false-fibers have been found to be reproducible between acquisitions (67,68). As this study has not explored the presence of false-fibers, it is unknown to what degree they contributed to the WM-like signal fraction.

An additional benefit provided by 3-tissue CSD methods is in the potential for tissue type specific masking. The CSF-like compartment presented in this paper is calculated as CSF-like diffusion in tissue by relying on the other compartments to identify which voxels were ‘tissue’. Unlike a binary tissue segmentation based on T1 intensity, calculations of WM- and

GM-like signal fraction compartments together were used to define voxels where 'tissue' composed a majority of signal from each voxel. This process relied exclusively on the single, native space diffusion image instead of reslicing and warping a separate structural image or atlas. Future studies might be able to take advantage of this approach by examining tissue compartment magnitudes inside voxels defined by the behavior of other tissue compartments. For example, tracking CSF-like (free water) tissue infiltration into voxels defined by the high proportion of WM-like tissue during aging or in certain pathological contexts.

## Conclusion

In this study, we performed a test-retest reliability and longer term stability analysis of the 3-tissue signal fractions as obtained from 3-tissue CSD techniques. We found that 3-tissue CSD technique provide reliable and stable estimates of tissue microstructure composition, up to 3 months longitudinally in a control population. This forms an important basis for further investigations utilizing 3-tissue CSD techniques to track changes in microstructure across a variety of conditions.

## Acknowledgements

NITRC, NITRC-IR, and NITRC-CE have been funded in whole or in part with Federal funds from the Department of Health and Human Services, National Institute of Biomedical Imaging and Bioengineering, the National Institute of Neurological Disorders and Stroke, under the following NIH grants: 1R43NS074540, 2R44NS074540, and 1U24EB023398 and previously GSA Contract No. GS-00F-0034P, Order Number HHSN268200100090U

## References

1. Basser PJ, Mattiello J, LeBihan D. MR diffusion tensor spectroscopy and imaging. Biophysical journal. 1994;66(1):259–267. [PubMed: 8130344]
2. Pierpaoli C, Basser PJ. Toward a quantitative assessment of diffusion anisotropy. Magnetic resonance in Medicine. 1996;36(6):893–906. [PubMed: 8946355]
3. Boullerne AI. The history of myelin. Experimental neurology. 2016;283;431–445. [PubMed: 27288241]
4. Le Bihan D, Mangin JF, Poupon C, Clark CA, Pappata S, Molko N, Chabriat H. Diffusion tensor imaging: concepts and applications. Journal of Magnetic Resonance Imaging. 2001;13(4);534–546. [PubMed: 11276097]
5. Nimsky C, Ganslandt O, Hastreiter P, Wang R, Benner T, Sorensen AG, Fahlbusch R. Preoperative and intraoperative diffusion tensor imaging-based fiber tracking in glioma surgery. Neurosurgery. 2005;56(1);130–138. [PubMed: 15617595]
6. Alexander AL, Lee JE, Lazar M, Field AS. Diffusion tensor imaging of the brain. Neurotherapeutics. 2007;4(3);316–329. [PubMed: 17599699]
7. Johansen-Berg H, Behrens TE. (Eds.). Diffusion MRI: from quantitative measurement to in vivo neuroanatomy. Academic Press 2013.
8. Wiegell MR, Larsson HB, Wedeen VJ. Fiber crossing in human brain depicted with diffusion tensor MR imaging. Radiology. 2000;217(3);897–903. [PubMed: 11110960]
9. Tuch DS, Reese TG, Wiegell MR, Wedeen VJ. Diffusion MRI of complex neural architecture. Neuron. 2003;40(5);885–895. [PubMed: 14659088]
10. Chenevert TL, Brunberg JA, Pipe JG. Anisotropic diffusion in human white matter: demonstration with MR techniques in vivo. Radiology. 1990;177(2);401–405. [PubMed: 2217776]
11. Jones DK, Cercignani M. Twenty-five pitfalls in the analysis of diffusion MRI data. NMR in Biomedicine. 2010;23(7);803–820. [PubMed: 20886566]

12. Roine T, Jeurissen B, Perrone D, Aelterman J, Leemans A, Philips W, Sijbers J. Isotropic non-white matter partial volume effects in constrained spherical deconvolution. Frontiers in neuroinformatics. 2014;8;28. [PubMed: 24734018]
13. Roine T, Jeurissen B, Perrone D, Aelterman J, Philips W, Leemans A, Sijbers J. Informed constrained spherical deconvolution (iCSD) Medical image analysis. 2015;24(1);269–281. [PubMed: 25660002]
14. Rydhög AS, Szczepankiewicz F, Wirestam R, Ahlgren A, Westin CF, Knutsson L, Pasternak O. Separating blood and water: perfusion and free water elimination from diffusion MRI in the human brain. Neuroimage. 2017;156;423–434. [PubMed: 28412443]
15. Jeurissen B, Leemans A, Tournier JD, Jones DK, Sijbers J. Investigating the prevalence of complex fiber configurations in white matter tissue with diffusion magnetic resonance imaging. Human brain mapping. 2013;34(11);2747–2766. [PubMed: 22611035]
16. Alexander AL, Hasan KM, Lazar M, Tsuruda JS, Parker DL. Analysis of partial volume effects in diffusion-tensor MRI. Magnetic Resonance in Medicine. 2001;45(5);770–780. [PubMed: 11323803]
17. Tournier JD, Mori S, Leemans A. Diffusion tensor imaging and beyond. Magnetic resonance in medicine. 2011;65(6);1532–1556. [PubMed: 21469191]
18. Assaf Y Pasternak O Diffusion tensor imaging (DTI)-based white matter mapping in brain research: a review. Journal of molecular neuroscience. 2008;34(1);51–61. [PubMed: 18157658]
19. Dell'Acqua F Tournier JD. Modelling white matter with spherical deconvolution: How and why?. NMR in Biomedicine. 2018;e3945. [PubMed: 30113753]
20. Tournier JD, Calamante F, Connelly A. Robust determination of the fibre orientation distribution in diffusion MRI: Non-negativity constrained super-resolved spherical deconvolution. NeuroImage. 2007;35(4);1459–1472. [PubMed: 17379540]
21. Raffelt D, Tournier JD, Rose S, Ridgway GR, Henderson R, Crozier S, Salvado O, Connelly A. Apparent fibre density: a novel measure for the analysis of diffusion-weighted magnetic resonance images. Neuroimage. 2012;59(4);3976–94. [PubMed: 22036682]
22. Jeurissen B, Tournier JD, Dhollander T, Connelly A, Sijbers J. Multi-tissue constrained spherical deconvolution for improved analysis of multi-shell diffusion data. Neuroimage. 2014;103;411–426 [PubMed: 25109526]
23. Dhollander T, Connelly A. A novel iterative approach to reap the benefits of multi-tissue CSD from just single-shell (+ b= 0) diffusion MRI data. In Proc ISMRM 2016. 2016;24;3010.
24. Dhollander T, Raffelt D, Connelly A. Towards interpretation of 3-tissue constrained spherical deconvolution results in pathology. Proceedings of the 25th International Society of Magnetic Resonance in Medicine. 2017;25;1815.
25. Mito R, Dhollander T, Raffelt D, Xia Y, Salvado O, Brodtmann A, Rowe CC, Villemagne VL, Connelly A. Investigating microstructural heterogeneity of white matter hyperintensities in Alzheimer's disease using single-shell 3-tissue constrained spherical deconvolution. Proceedings of the 26th annual meeting of the International Society of Magnetic Resonance in Medicine 2018. 2018;135. doi:10.1101/623124
26. Mito R, Dhollander T, Xia Y, Raffelt D, Salvado O, Churilov L, Rowe CC, Brodtmann A, Villemagne VL, Connelly A. In vivo microstructural heterogeneity of white matter lesions in Alzheimer's disease using tissue compositional analysis of diffusion MRI data. bioRxiv. 2019;623124. doi: 10.1101/623124
27. Aerts H, Dhollander T, Marinazzo D. Evaluating the performance of 3-tissue constrained spherical deconvolution pipelines for within-tumor tractography. bioRxiv. 2019;629873. doi: 10.1101/629873
28. Pasternak O, Sochen N, Gur Y, Intrator N, Assaf Y. Free water elimination and mapping from diffusion MRI. Magnetic Resonance in Medicine. 2009;62(3);717–730. [PubMed: 19623619]
29. Albi A, Pasternak O, Minati L, Marizzoni M, Bartrés-Faz D, Bargalló N, Bosch B, Rossini PM, Marra C, Müller B, Fiedler U. Free water elimination improves test–retest reproducibility of diffusion tensor imaging indices in the brain: a longitudinal multisite study of healthy elderly subjects. Human brain mapping. 2017;38(1);12–26. [PubMed: 27519630]

30. Zhang H, Schneider T, Wheeler-Kingshott CA, Alexander DC. NODDI: practical in vivo neurite orientation dispersion and density imaging of the human brain. Neuroimage. 2012;61(4);1000–1016. [PubMed: 22484410]
31. Pasternak O, Kelly S, Sydnor VJ, Shenton ME. Advances in microstructural diffusion neuroimaging for psychiatric disorders. NeuroImage. 2018;182(1);259–282. [PubMed: 29729390]
32. Biswal BB, Mennes M, Zuo XN, Gohel S, Kelly C, Smith SM, Beckmann CF, Adelstein JS, Buckner RL, Colcombe S, Dogonowski AM. Toward discovery science of human brain function. Proceedings of the National Academy of Sciences. 2010;107(10);4734–9.
33. 1000 Functional Connectomes Project (http://www.nitrc.org/projects/fcon_1000/); Nathan S. Kline Institute for Psychiatric Research (NKI), enhanced NKI (eNKI) test–retest data.
34. Nooner KB, Colcombe S, Tobe R, Mennes M, Benedict M, Moreno A, Panek L, Brown S, Zavitz S, Li Q, Sikka S. The NKI-Rockland sample: a model for accelerating the pace of discovery science in psychiatry. Frontiers in neuroscience. 2012;6:152. [PubMed: 23087608]
35. Oscar-Berman M, Marinković K. Alcohol: effects on neurobehavioral functions and the brain. Neuropsychology review. 2007;17(3);239–257. [PubMed: 17874302]
36. Jiang J, Zhao YJ, Hu XY, Du MY, Chen ZQ, Wu M, Li KM, Zhu HY, Kumar P, Gong QY. Microstructural brain abnormalities in medication-free patients with major depressive disorder: a systematic review and meta-analysis of diffusion tensor imaging. Journal of psychiatry neuroscience: JPN. 2017;42(3);150. [PubMed: 27780031]
37. Reynolds BB, Stanton AN, Soldozy S, Goodkin HP, Wintermark M, Druzgal TJ. Investigating the effects of subconcussion on functional connectivity using mass-univariate and multivariate approaches. Brain imaging and behavior. 2017;1–14. [PubMed: 26780240]
38. Veraart J, Novikov DS, Christiaens D, Ades-Aron B, Sijbers J, Fieremans E. Denoising of diffusion MRI using random matrix theory. NeuroImage. 2016;142;394–406. [PubMed: 27523449]
39. Kellner E, Dhital B, Kiselev VG, Reisert M. Gibbs‐ringing artifact removal based on local subvoxel‐shifts. Magnetic resonance in medicine. 2016;76(5);1574–1581. [PubMed: 26745823]
40. Smith SM, Jenkinson M, Woolrich MW, Beckmann CF, Behrens TE, Johansen-Berg H, Bannister PR, De Luca M, Drobnjak I, Flitney DE, Niazy RK. Advances in functional and structural MR image analysis and implementation as FSL. Neuroimage. 2004;23;S208–19. [PubMed: 15501092]
41. Andersson JL, Skare S, Ashburner J. How to correct susceptibility distortions in spin-echo echo-planar images: application to diffusion tensor imaging. Neuroimage. 2003;20(2);870–888. [PubMed: 14568458]
42. Andersson JL, Sotiropoulos SN. An integrated approach to correction for off-resonance effects and subject movement in diffusion MR imaging. Neuroimage. 2016;125;1063–1078. [PubMed: 26481672]
43. Andersson JL, Graham MS, Zsoldos E, Sotiropoulos SN. Incorporating outlier detection and replacement into a non-parametric framework for movement and distortion correction of diffusion MR images. NeuroImage. 2016;141;556–572. [PubMed: 27393418]
44. Greenspan H Super-resolution in medical imaging. The Computer Journal. 2008;52(1);43–63.
45. Kuklisova-Murgasova M, Quaghebeur G, Rutherford MA, Hajnal JV, Schnabel JA. Reconstruction of fetal brain MRI with intensity matching and complete outlier removal. Medical image analysis. 2012;16(8);1550–1564. [PubMed: 22939612]
46. Bastiani M, Andersson JL, Cordero-Grande L, Murgasova M, Hutter J, Price AN, Makropoulos A, Fitzgibbon SP, Hughes E, Rueckert D, Victor S. Automated processing pipeline for neonatal diffusion MRI in the developing human connectome project. NeuroImage. 2019;185;750–763. [PubMed: 29852283]
47. Pietsch M, Christiaens D, Hutter J, Cordero-Grande L, Price AN, Hughes E, Edwards AD, Hajnal JV, Counsell SJ, Tournier JD. A framework for multi-component analysis of diffusion MRI data over the neonatal period. NeuroImage. 2018.
48. Avants BB, Tustison NJ, Stauffer M, Song G, Wu B, Gee JC. The Insight ToolKit image registration framework. Frontiers in Neuroinformatics, 2014;8;44. [PubMed: 24817849]
49. Dhollander T, Raffelt D, Connelly A. Unsupervised 3-tissue response function estimation from single-shell or multi-shell diffusion MR data without a co-registered T1 image. In ISMRM Workshop on Breaking the Barriers of Diffusion MRI. 2016;(5).

50. Raffelt D, Tournier JD, Fripp J, Crozier S, Connelly A, Salvado O. Symmetric diffeomorphic registration of fibre orientation distributions. NeuroImage. 2011;56(3);1171–1180. [PubMed: 21316463]

51. Shattuck DW, Mirza M, Adisetiyo V, Hojatkashani C, Salamon G, Narr KL, Poldrack RA, Bilder RM, Toga AW. Construction of a 3D probabilistic atlas of human cortical structures. Neuroimage. 2008;39(3);1064–80. [PubMed: 18037310]

52. Avants BB, Tustison N, Song G. Advanced normalization tools (ANTS). Insight j, 2009;2;1–35.

53. Tournier JD, Smith RE, Raffelt DA, Tabbara R, Dhollander T, Pietsch M, Christiaens D, Jeurissen B, Yeh CH, Connelly A. MRtrix3: A fast, flexible and open software framework for medical image processing and visualisation. bioRxiv. 2019;551739. doi:10.1101/551739

54. Jenkinson M, Beckmann CF, Behrens TEJ, Woolrich MW, Smith SM. FSL. NeuroImage 2012;62(2);782–790. [PubMed: 21979382]

55. Pedraza O, Bowers D, Gilmore R. Asymmetry of the hippocampus and amygdala in MRI volumetric measurements of normal adults. Journal of the International Neuropsychological Society. 2004;10(5):664–78. [PubMed: 15327714]

56. Ofori E, DeKosky ST, Febo M, Colon-Perez L, Chakrabarty P, Duara R, Adjouadi M, Golde TE, Vaillancourt DE, Alzheimer's Disease Neuroimaging Initiative. Free-water imaging of the hippocampus is a sensitive marker of Alzheimer's disease. NeuroImage: Clinical. 2019;22;101985.

57. Ofori E, Pasternak O, Planetta PJ, Li H, Burciu RG, Snyder AF, Lai S, Okun MS, Vaillancourt DE. Longitudinal changes in free-water within the substantia nigra of Parkinson's disease. Brain. 2015;138(8);2322–31. [PubMed: 25981960]

58. Burciu RG, Ofori E, Shukla P, Pasternak O, Chung JW, McFarland NR, Okun MS, Vaillancourt DE. Free‐water and BOLD imaging changes in Parkinson's disease patients chronically treated with a MAO‐B inhibitor. Human brain mapping. 2016;37(8);2894–903. [PubMed: 27089850]

59. Pasternak O, Westin CF, Bouix S, Seidman LJ, Goldstein JM, Woo TU, Petryshen TL, Mesholam-Gately RI, McCarley RW, Kikinis R, Shenton ME. Excessive extracellular volume reveals a neurodegenerative pattern in schizophrenia onset. Journal of Neuroscience. 2012 11 28;32(48);17365–72. [PubMed: 23197727]

60. Mandl RC, Pasternak O, Cahn W, Kubicki M, Kahn RS, Shenton ME, Pol HEH. Comparing free water imaging and magnetization transfer measurements in schizophrenia. Schizophrenia research; 2015;161(1);126–132. [PubMed: 25454797]

61. Pasternak O, Koerte IK, Bouix S, Fredman E, Sasaki T, Mayinger M, Helmer KG, Johnson AM, Holmes JD, Forwell LA, Skopelja EN. Hockey Concussion Education Project, Part 2. Microstructural white matter alterations in acutely concussed ice hockey players: a longitudinal free-water MRI study. Journal of neurosurgery. 2014;120(4);873–81. [PubMed: 24490785]

62. Chamberland M, Iqbal NS, Rudrapatna SU, Parker G, Tax CM, Staffurth J, Powell J, Wise R, Jones DK. Characterising tissue heterogeneity in cerebral metastases using multi-shell multi-tissue constrained spherical deconvolution. Proceedings of the 27th International Society of Magnetic Resonance in Medicine. 2019;27;3613.

63. Parker GD, Marshall D, Rosin PL, Drage N, Richmond S, Jones DK. A pitfall in the reconstruction of fibre ODFs using spherical deconvolution of diffusion MRI data. Neuroimage. 2013;65;433–448. [PubMed: 23085109]

64. Ning L, Laun F, Gur Y, DiBella EV, Deslauriers-Gauthier S, Megherbi T, Ghosh A, Zucchelli M, Menegaz G, Fick R, St-Jean S. Sparse Reconstruction Challenge for diffusion MRI: Validation on a physical phantom to determine which acquisition scheme and analysis method to use?. Medical image analysis. 2015;26(1);316–31. [PubMed: 26606457]

65. Wilkins B, Lee N, Gajawelli N, Law M, Leporé N. Fiber estimation and tractography in diffusion MRI: development of simulated brain images and comparison of multi-fiber analysis methods at clinical b-values. Neuroimage. 2015;109;341–356. [PubMed: 25555998]

66. Schilling KG, Janve V, Gao Y, Stepniewska I, Landman BA, Anderson AW. Histological validation of diffusion MRI fiber orientation distributions and dispersion. NeuroImage. 2018;165;200–221. [PubMed: 29074279]

67. Maier-Hein KH, Neher PF, Houde JC, Côté MA, Garyfallidis E, Zhong J, Chamberland M, Yeh FC, Lin YC, Ji Q, Reddick WE. The challenge of mapping the human connectome based on diffusion tractography. Nature communications. 2017;8(1);1349.

68. Roine T, Jeurissen B, Perrone D, Aelterman J, Philips W, Sijbers J, Leemans A. Reproducibility and intercorrelation of graph theoretical measures in structural brain connectivity networks. Medical image analysis. 2019;52;56–67. [PubMed: 30471463]

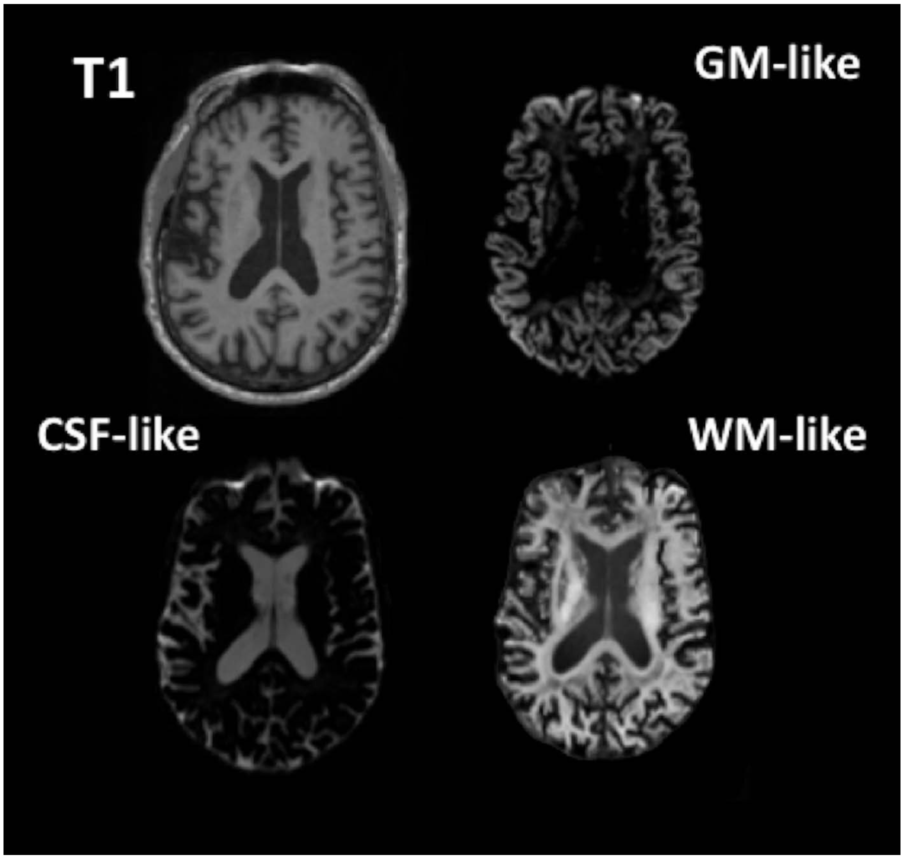

**Figure 1:**

Axial slices showing a T1-weighted MPRAGE and the GM-, CSF-, and WM-like tissue compartments derived from the dMRI data using 3-tissue CSD.

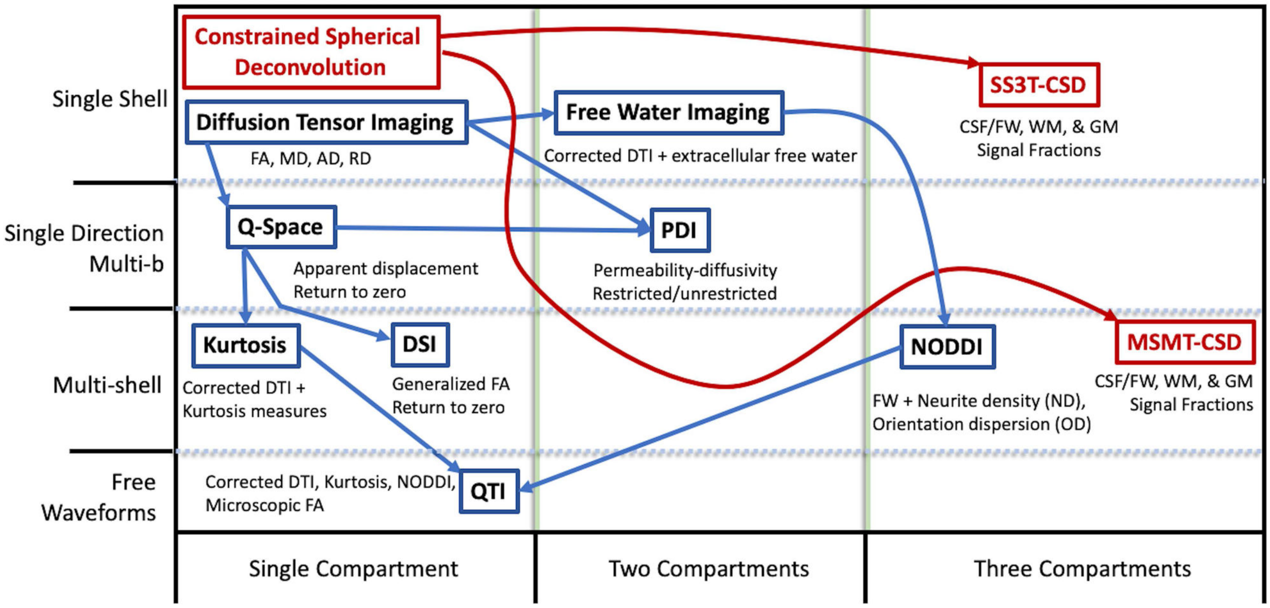

**Figure 2:**

Chart adapted from Pasternak et al.(31); comparison of common DTI and other model metrics to CSD derived tissue signal fractions by requirements of acquisition (rows) and number of output compartments (columns). Methods derived from CSD have been added in red.

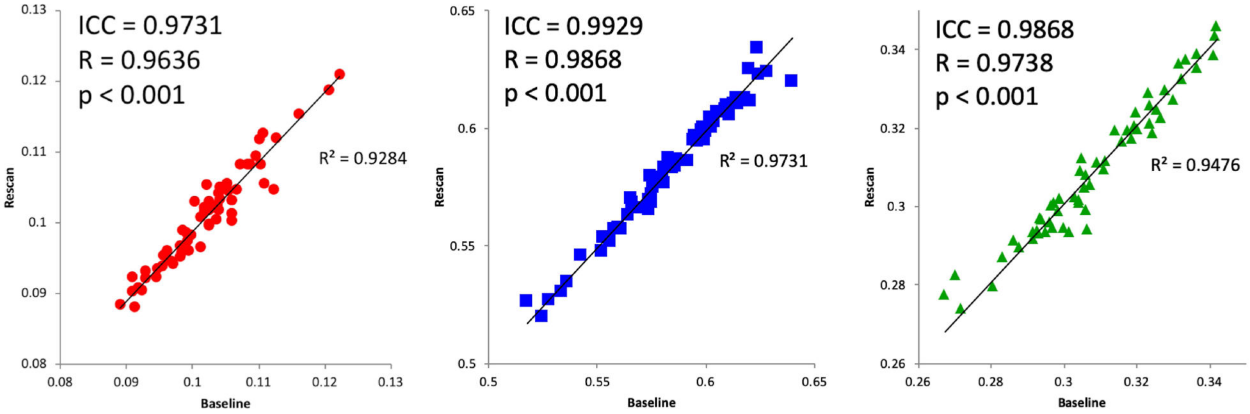

**Figure 3:**

*Immediate rescan* baseline and re-scan values for CSF- (left), WM- (center), and GM-like (right) signal fractions obtained from a cohort scanned with a duplicate sequence immediately following baseline. Includes ICC and Pearson’s correlation values.

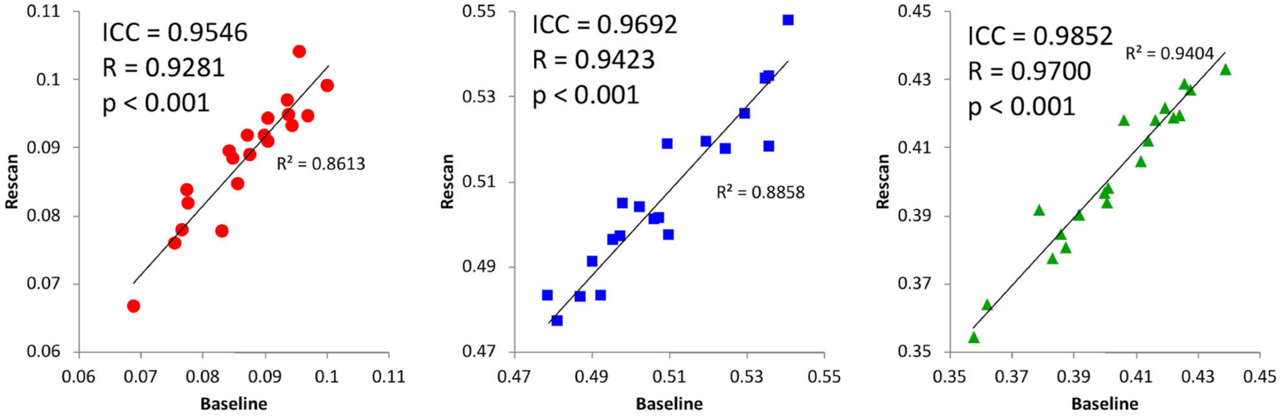

**Figure 4:**

*Short timescale* baseline and re-scan values from CSF- (left), WM- (center), and GM-like (right) signal fractions obtained from a cohort with 7–60 days between baseline and re-scan. Subjects were taken from the eNKI group and their single-shell dMRI data analyzed with SS3T-CSD. Includes ICC and Pearson’s correlation values.

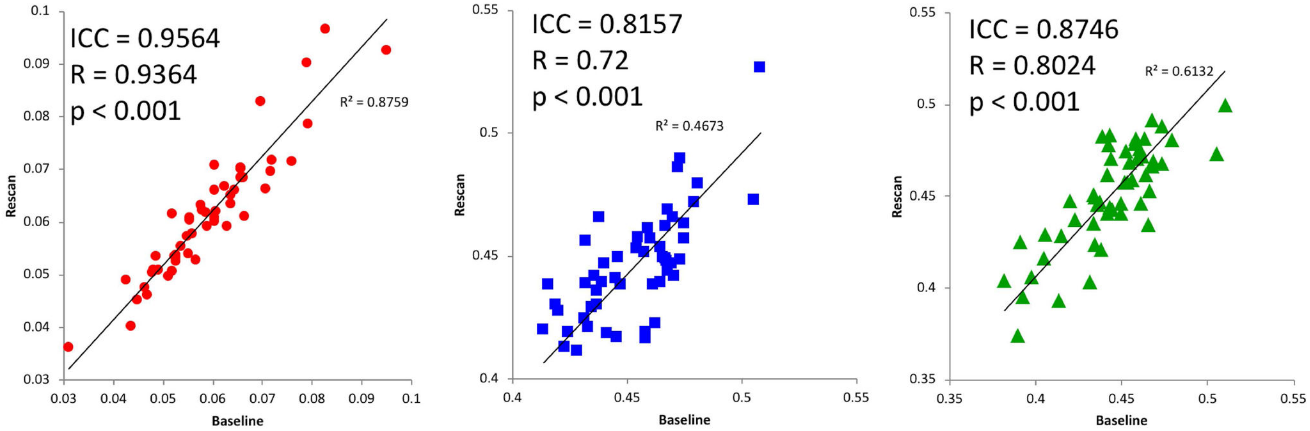

**Figure 5:**

*Long timescale* baseline and re-scan values from CSF- (left), WM- (center), and GM-like (right) signal fractions obtained from a cohort with 3 months between baseline and re-scan. Includes ICC and Pearson’s correlation values.

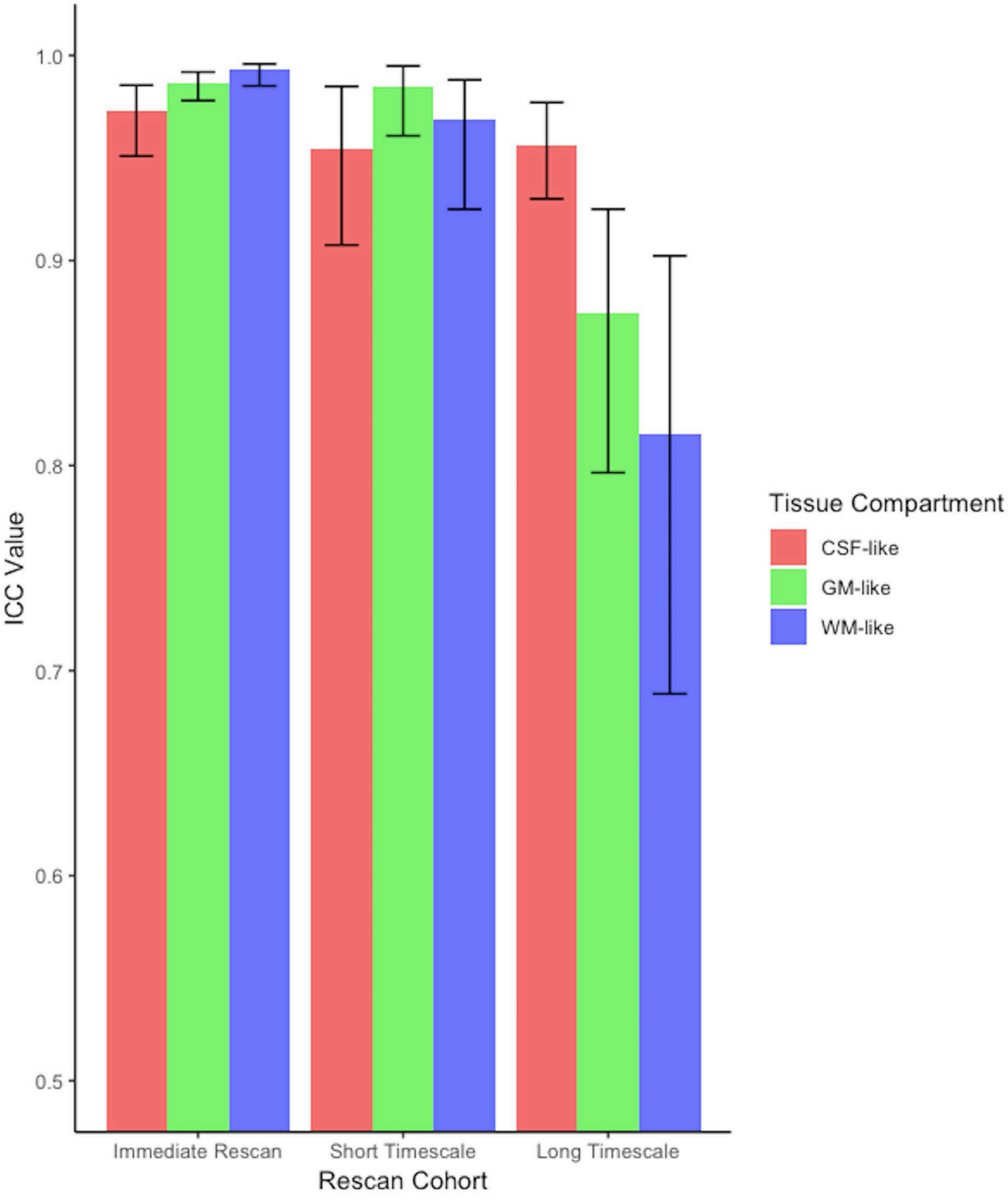

**Figure 6:**

Results from parametric ICC bootstrapping with ICC calculated from subject data (Table 1) and 95% confidence intervals displayed. There was overlap between the 95% confidence intervals from each cohort's CSF-like ICC but in the *long-timescale* group the WM-like and GM-like signal fraction ICC did not overlap with either other cohort.

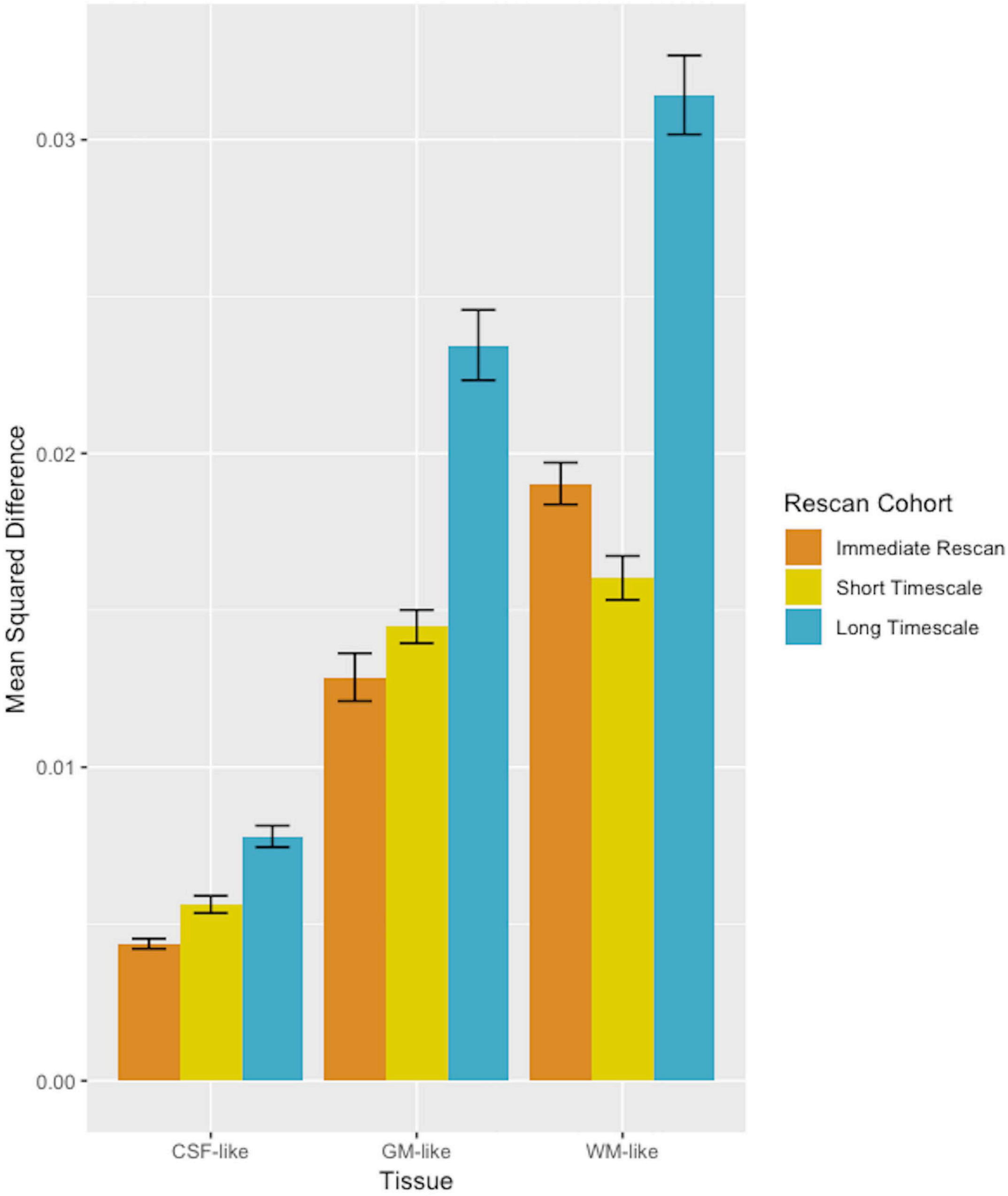

**Figure 7:**

Bar plot (±SE) displaying the mean squared difference between scan and rescan, averaged across individuals for each tissue map and in each cohort. Comparison between *different* tissues' mean squared differences is discouraged however, as the average absolute value of each voxel and the distribution of values across the brain is highly different for different tissue types.

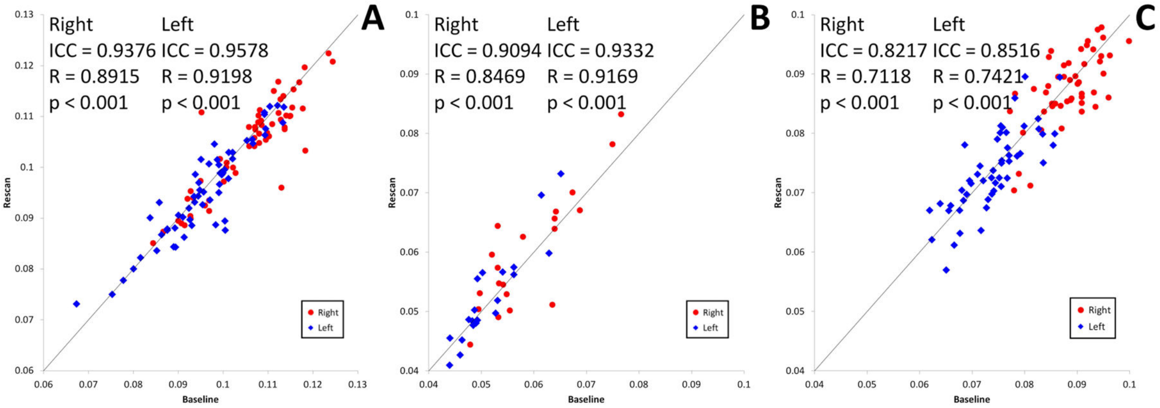

**Figure 8:**

(A) CSF-like signal fraction for the left and right hippocampus in the 59 pairs of baseline-retest scans in the *immediate rescan* cohort. Values for the right hippocampus of each individual are shown in red and values for the left hippocampus are shown in blue. (B) CSF-like signal fraction for the left and right hippocampus in the 20 pairs of baseline-retest scans in the *short timescale* cohort. Values for the right hippocampus of each individual are shown in red and values for the left hippocampus are shown in blue. (C) CSF-like signal fraction for the left and right hippocampus in the 52 pairs of baseline-retest scans in the *long timescale* cohort. Values for the right hippocampus of each individual are shown in red and values for the left hippocampus are shown in blue.

## Table 1:

Statistical analysis of the 3 test-retest cohorts in the experiment; p-values are calculated based on the Pearson's correlation. For each cohort the left hippocampus (LH) and right hippocampus (RH) were selected as ROIs and the CSF-like (free water) signal-fraction was measured to examine the reliability of 3-tissue CSD derived free water estimates in subcortical structures specifically as well.

| Dataset | Tissue | Subjects | ICC | Pearson's Rho | p-value |
|---|---|---|---|---|---|
| *Immediate rescan* | CSF-like | 59 | 0.9731 | 0.9636 | <0.001 |
| | WM-like | 59 | 0.9929 | 0.9868 | <0.001 |
| | GM-like | 59 | 0.9868 | 0.9748 | <0.001 |
| | LH CSF-like | 59 | 0.9578 | 0.9181 | <0.001 |
| | RH CSF-like | 59 | 0.9376 | 0.8915 | <0.001 |
| *Short timescale (7–60 days)* | CSF-like | 20 | 0.9546 | 0.9281 | <0.001 |
| | WM-like | 20 | 0.9692 | 0.9423 | <0.001 |
| | GM-like | 20 | 0.9852 | 0.9700 | <0.001 |
| | LH CSF-like | 20 | 0.9332 | 0.9169 | <0.001 |
| | RH CSF-like | 20 | 0.9094 | 0.8469 | <0.001 |
| *Long timescale (3–4 months)* | CSF-like | 52 | 0.9564 | 0.9364 | <0.001 |
| | WM-like | 52 | 0.8157 | 0.7200 | <0.001 |
| | GM-like | 52 | 0.8746 | 0.8024 | <0.001 |
| | LH CSF-like | 52 | 0.8516 | 0.7421 | <0.001 |
| | RH CSF-like | 52 | 0.8217 | 0.7118 | <0.001 |